Available online at www.sciencedirect.com
SCIENCE DIRECT®
Remote Sensing of Environment 89 (2004) 29–40
Remote Sensing of Environment
www.elsevier.com/locate/rse

Laboratory and field measurements of the modification of radar backscatter by sand

Kevin K. Williams*, Ronald Greeley

Department of Geological Sciences, Arizona State University, Tempe, AZ 85287-1404, USA

Received 29 July 2002; received in revised form 19 September 2003; accepted 19 September 2003

Abstract

Over the last two decades, the use of synthetic aperture radar (SAR) to address geologic problems has expanded as new applications for radar have been developed. One of the earliest and perhaps most surprising results from orbital SAR images of the Sahara was that, under certain conditions, radar signals penetrated up to several meters of sand to reveal subsurface features such as ancient river channels. Subsequent studies of radar penetration of arid sand deposits have dealt with factors that govern the ability of radar to penetrate a sand cover. This paper presents results from a laboratory experiment in which radar backscatter from a surface of rocks was measured under controlled conditions as a function of frequency, polarization, incidence angle, and sand cover thickness. The sand used in the experiment had a moisture content of 0.28 vol.% and caused calculated average attenuations of 4.2 ± 1 dB/m for C-band and $\sim 11 \pm 2$ dB/m for X-band. Results from the experiment were compared to field measurements of sand thickness during acquisition of airborne radar images. In AIRSAR images, the extent of dry sand in a dune field appears best in C-band because longer wavelength L- and P-band signals penetrate thinner sand deposits. Images of wet sand (4.9 vol.%) suggest that L-band was able to penetrate thin sand even though that sand was wet. Together, these laboratory and field measurements contribute towards a better understanding of how a sand cover modifies the radar backscatter of a surface.

Keywords: Radar backscatter; SAR; Radar penetration; AIRSAR; Sand

1. Introduction

Synthetic aperture radar (SAR) has become an increasingly useful remote sensing tool for studying geology on Earth. Orbital and airborne SAR instruments operating at multiple frequencies and polarizations [e.g., SIR-C/X-SAR (Jordan, Huneycutt, & Werner, 1995) and AIRSAR (Lou et al., 2001)] have returned radar images that provide more information about a target than single frequency and polarization systems. These data can be used to classify surface types based on surface roughness, and they offer insight into the potential for subsurface imaging at various frequencies (e.g., Dabbagh, Al-Hinai, & Khan, 1997; Schaber & Breed, 1999).

The ability of radar to penetrate loose material such as sand and alluvium is beneficial to studies of the geologic and climatic history of an area. An early study (Dellwig, 1969) showed that P-band ($v = 0.5$ GHz; $\lambda = 60$ cm) radar had potential for penetrating loose deposits. Subsurface imaging by radar gained widespread attention when images from the 1981 NASA Shuttle Imaging Radar mission (SIR-A) revealed buried river channels beneath the sand of the Sahara (McCauley et al., 1982). River channels appeared as dark, dendritic patterns in L-band ($v = 1.25$ GHz; $\lambda = 24$ cm) images, and sand-covered bedrock returned a bright radar signal (McCauley et al., 1982, 1986). Related field studies revealed that the radar signals were able to penetrate up to 1–2 m of very dry sand to return a signal from buried bedrock and calcium carbonate-cemented nodules (McCauley et al., 1986; Schaber, McCauley, Breed, & Olhoeft, 1986). The dark radar response from the channels was caused by reflection of the radar signal from smoother channel fill material and by attenuation of the signal by that material (Breed et al., 1983; Davis, Breed, McCauley, & Schaber, 1993;

* Corresponding author. Center for Earth and Planetary Studies, National Air and Space Museum, Smithsonian Institution, Washington, DC 20013-7012, USA. Tel.: +1-202-633-2487; fax: +1-202-786-2566.
E-mail address: williamsk@nasm.si.edu (K.K. Williams).

0034-4257/$ - see front matter © 2003 Elsevier Inc. All rights reserved.
doi:10.1016/j.rse.2003.09.006

Elachi, Roth, & Schaber, 1984; McCauley et al., 1982, 1986; Schaber et al., 1986). Schaber et al. (1986) note that the modern sand sheet in the Eastern Sahara now covers much of the region, but the L-band radar of SIR-A was able to penetrate sand cover to expose previously obscured information about past fluvial activity.

After detection of subsurface penetration by radar during SIR-A, older SEASAT radar data (also L-band) were reconsidered, and it was found that SEASAT data exposed subsurface tectonic and geomorphic features in southern California (Blom, Crippen, & Elachi, 1984). Radar penetration field studies were also planned to coincide with and to take advantage of data from the second Shuttle Imaging Radar mission (SIR-B) in 1984. Farr, Elachi, Hartl, and Chowdhury (1986) placed receivers at several depths in the Nevada desert and measured power received as SIR-B passed overhead. The data were processed to determine attenuation of the signal as it passed through alluvium in the area. The results of Farr et al. were significant because they showed that radar can penetrate desert soils even in regions where soil moisture is greater than in hyperarid regions such as the Sahara (Table 1). SIR-B also provided the opportunity to conduct further field measurements of sand thickness in areas where radar could penetrate the sand. Berlin, Tarabzouni, Al-Naser, Sheikho, and Larson (1986) studied an area in Saudi Arabia and compared their measurements of sand thickness to the L-band images from SIR-A (Fig. 1) and SIR-B. They found that the radar signal penetrated as much as 1.25 m of sand to return an image of the subsurface. They also determined that the radar was unable to penetrate ~ 3 m of sand accumulated in a sand hill (Fig. 1). Measurements such as these from SIR-A and SIR-B began to demonstrate the ability of L-band radar to image subsurface geology and return information that is otherwise obscured from optical sensors such as LANDSAT and orbital photographs. The need for multifrequency imaging radar systems was recognized and led to the two SIR-C/X-SAR missions in April and October 1994.

The United States component of the mission (SIR-C) included L-band ($\nu = 1.25$ GHz; $\lambda = 24$ cm) and C-band ($\nu = 5.3$ GHz; $\lambda = 5.6$ cm) radars that were fully polarimetric, with the ability to transmit and receive in both horizontal and vertical polarizations (Jordan et al., 1995). The German/Italian component of the mission (X-SAR) was an X-band

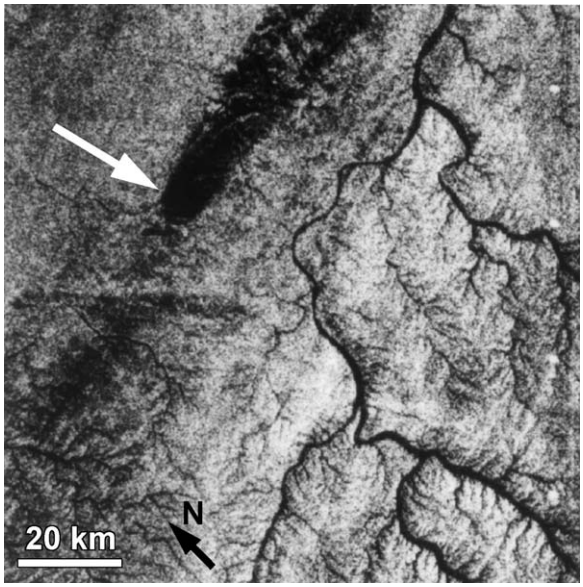

Fig. 1. SIR-A image over the Al Labbah Plateau, Saudi Arabia, where L-band radar penetrated ~1.25 m of sand to reveal dendritic patterns but did not penetrate 3 m of sand in a sand hill (arrow) (SIR-A data take no. 28).

($\nu = 9.6$ GHz; $\lambda = 3.1$ cm) radar operating in VV polarization (Jordan et al., 1995). SIR-C/X-SAR had the added benefit of variable incidence angle.

Also in the early 1990s, the Magellan mission (Saunders et al., 1992) used S-band ($\nu = 2.385$ GHz; $\lambda = 12.6$ cm) to penetrate the thick cloud cover of Venus to return a radar map of the surface. Imaging radars are also likely to continue playing an important role in future studies of the Earth and the other planets. For example, an imaging radar mission to Mars would have the potential to map the bedrock geology of that planet (e.g., Campbell et al., 2001) by penetrating sand and dust that obscures much of the surface at visible and thermal wavelengths. Table 2 lists characteristics of some orbital and airborne imaging radar systems that have been used for geological studies over the last 25 years.

In a comparison of sand penetration by radar at various frequencies, Schaber and Breed (1999) noted the need for a better understanding of how sand affects a radar image at various radar parameters. To address this issue, experimental measurements of the radar backscatter coefficient under controlled conditions were conducted. The experimental results were then compared to backscatter values acquired by the NASA/JPL AIRSAR instrument during two cam-

Table 1
Comparison of volumetric moisture contents in radar penetration studies

Location	Study	Experiment	Moisture content[a] (%)
Sahara	Schaber et al., 1986	SIR-A	< 1.0
Saudi Arabia	Berlin et al., 1986	SIR-B	0.29–0.30
Nevada desert	Farr et al., 1986	SIR-B	4.2–6.9
Laboratory	this study	backscatter	0.28
Mojave Desert	this study	1999 AIRSAR	4.9
Mojave Desert	this study	2000 AIRSAR	0.26

[a] Moisture content is given as volume percent.

Table 2
Characteristics of imaging radars

Sensor	Band	Wavelength (cm)	Frequency (GHz)
X-SAR	X	3.1	9.6
SIR-C, RADARSAT, AIRSAR	C	5.8	5.3
MAGELLAN	S	12.6	2.385
SEASAT, SIR-A, -B, -C, AIRSAR	L	23.5	1.25
AIRSAR	P	68	0.44

paigns coordinated with field measurements of sand thickness and surface properties.

2. Laboratory measurements of backscatter

2.1. Overview

In order to understand better how a cover of sand modifies backscatter, an experiment was conducted to measure the change in radar backscatter of a surface as layers of sand were added. The Telecommunications Research Center at Arizona State University houses a large electromagnetic anechoic chamber with a radar emitter/receiver system able to operate at frequencies that include those of imaging radar at 0.5–12 GHz (Birtcher, 1992). The availability of the chamber presented an excellent opportunity to measure the change in radar backscatter for varying radar properties under controlled conditions. Although the facility is typically used to measure radar cross section of aerospace objects such as helicopter models (C. Birtcher, personal communication), the anechoic chamber was reconfigured to measure backscatter over geologic materials.

The experiment consisted of a target table that held a rough surface of rounded river gravel (~ 2.5 cm diameter) that was later covered with sand. The radar emitter and receiver were oriented downward and were suspended over the target on a positioning system that allowed measurements at various incidence angles (Fig. 2).

Backscatter measurements were acquired at incidence angles from −10° to 60° from nadir at 0.2° increments. Measurements were made over radar frequencies centered at 5.3 (C-band) and 9.7 GHz (X-band). Each frequency range spanned 3 GHz and consisted of 201 measurements. In addition, orientations of the radar emitter and receiver were adjusted to collect data at HH (horizontally transmitted, horizontally received), HV (horizontally transmitted, vertically received), and VV (vertically transmitted, vertically received) polarizations. Table 3 lists parameters that were varied during the experiment. Although lower radar frequencies would have been able to penetrate thicker sand, the dimensions of the experiment prevented use of the equipment necessary for measurements at lower frequencies.

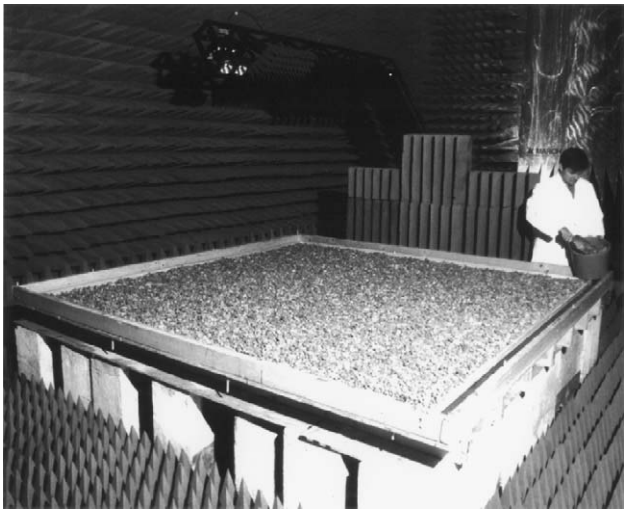

Fig. 2. Experiment configuration showing radar emitter and receiver above the initial target of river gravel before sand was added.

Table 3
Laboratory parameters for backscatter measurements

Parameter	Range of measurements	Increment
Frequency	C-band (3.65–6.35 GHz)	0.0135 GHz
	X-band (8.18–11.18 GHz)	0.015 GHz
Polarization	HH, HV, VV	–
Incidence angle	−10–60°	0.2°
Sand thickness	0–23.2 cm[a]	varies

[a] Specific values of sand thickness: 0, 0.3, 0.5, 1.5, 3.1, 5.8, 8.7, 11.6, 17.4, and 23.2 cm.

2.2. Experimental setup and calibration

Fig. 2 shows the configuration of the experiment with the radar emitter and receiver suspended above the target. A 3 × 3-m table was constructed of dry lumber held together with wooden dowels and served as a platform for the gravel and sand. This table was supported above the floor by dense foam blocks so that it was at the center of rotation of the incidence angle positioning system. The rocks were confined to a target area of 2.75 × 2.75 m over which sand was emplaced. Overflow of sand due to its natural angle of repose extended to the table edge.

Before gravel and sand were added to the table, calibration measurements were made for all radar parameter variations. A 5-cm-thick deposit of rounded river gravel was then added to act as the initial, sand-free target. The gravel had an average diameter of 2.5 cm and had been rinsed several times and dried to remove any dust that could contain clay particles and have an effect on the radar backscatter. The gravel was also sorted and inspected to remove angular fragments and vesicular basalts. By designing the experiment so that the top of the rock surface was at the center of rotation of the positioning system, the center of the targeted radar energy remained stationary as incidence angle was varied.

The sand used in the experiment was '#60 Silver Sand' acquired from P.W. Gillibrand of Simi Valley, CA. A sieve analysis showed that 96% of the sand had a grain size of 0.1–0.3 mm with 60% having a grain size from 0.2 to 0.3 mm. Thus, the sand is similar in grain size to sand classified as the modern aeolian sand sheet, lower aeolian sand sheet, and medium-sand alluvium in the Sahara studies of McCauley et al. (1986) and Schaber et al. (1986). The sand was composed mineralogically of ~ 80% quartz, ~ 16% feldspar, and ~ 4% lithic fragments and other minerals. Al-

though the sand is not pure quartz, the backscatter over a small sample of the #60 Silver Sand was measured and compared to the backscatter over a sample of pure quartz sand. The difference between the two measurements was negligible and verifies that the #60 Silver Sand can be used for this experiment without errors introduced by non-quartz components.

Because moisture content of sand affects its electrical properties and the ability of radar to penetrate it, the moisture content was measured before and throughout the experiment by weighing samples before and after heating to remove moisture. Although the water weight was measured in grams, an average sand density of 1.47 g/cm^3 was used to convert to volume percent of moisture for comparison to other studies of radar attenuation (e.g., Farr et al., 1986). The amount of moisture in the sand used for this experiment was measured at 0.28 ± 0.1 vol.%. This is much less moisture than was measured in Nevada by Farr et al. (1986), but is approximately the same moisture level measured in Saudi Arabia (Berlin et al., 1986) (Table 1). The sand was further characterized by having its dielectric properties measured. Complex permittivity measurements were used to constrain the real permittivity, ε', at 2.08 for C-band and 1.97 for X-band. The extreme dryness of the sand leads to a low imaginary permittivity, ε', which, because of uncertainties in measurements, is constrained at 0.01–0.02 for both C-band and X-band.

2.3. Measurements

Following the calibration measurements, backscatter of the river gravel was measured at all combinations of radar frequency, polarization, and incidence angle (Table 3). In order to cover the frequency ranges at C-band and X-band, two radar emitter/receiver sets were used. To make measurements at the three polarization combinations, orientations of the emitter/receiver sets were adjusted. Therefore, six sweeps through the range of incidence angles were needed to cover the full suite of measurements at each sand thickness level (starting with no sand).

When bare rock measurements were completed, sand was added to the first level. The sand was added in such a way to prevent packing that could create inhomogeneities in density. Because the area of the target table prevented access from all sides, a walkway was constructed that spanned the area at a height that would clear the highest sand level. The walkway was mounted on wheels so that it could be moved easily across the sample area, and it was removed from the chamber prior to measurements. In order to add sand to consistent levels over the target area, metal guide bars were attached to the sides of the table, and a screen box was placed on the guide bars. The screen box served as an indicator of the level to which sand was to be added. After sand was added across the table in this manner, a metal straight edge was pulled across the guide bars to level the sand, and the metal guide bars were removed before measurements were made. This technique was used to add sand to nine thickness levels up to 23.2 cm (Table 3). The combinations of frequency, polarization, incidence angle, and sand thickness led to 4.25 million data points.

2.4. Data analysis

The raw data were processed to remove extraneous signals from the anechoic chamber, and the received signal was gated over a time range corresponding to the expected receipt time for the target. Calibration measurements were then applied to give backscatter results in decibels per square meter. The calibrated data display variations due to constructive and destructive interference likely caused by the target gravel moving in and out of phase as measurements vary over frequency range and incidence angle (J. van Zyl, personal communication). Laboratory backscatter measurements are typically performed as the target is rotated in the horizontal plane (Nesti, Fortuny, & Lopez-Sanchez, 2000), and the results are averaged to remove effects of noise and variations in target shape. Because it was not possible to rotate the target in this experiment, data are averaged over frequency and incidence angle to determine how backscatter varies. Several averaging techniques were tested with respect to preserving the information in the original data, and it was found that averaging over 0.1 GHz in frequency and 5° in incidence angle could be applied (Fig. 3). In addition, data from $-10°$ to 10° in incidence angle were averaged to compensate for some of the single-orientation effects.

For each combination of radar band, polarization, and incidence angle, the averaged backscatter data were plotted as a function of frequency for the various sand levels. Because the sand was dry, a linear curve was fit to the change in backscatter as a function of frequency. These data could then be used to plot backscatter as a function of sand thickness for any selected frequency within the C- and X-band ranges measured in this study (e.g., Fig. 4). Because the radar signal is refracted as it passes into the sand layer at an angle, a dielectric constant of $\varepsilon' = 2$ was used to calculate the path length. The path length is used for sand thickness in the backscatter versus thickness plots (for sand thickness >0). These data were plotted as change in backscatter versus sand thickness by subtracting the backscatter at each sand level from the backscatter at the first sand level (0.3 cm). Linear curves were then fit to these plots, and those curves were used to calculate the attenuation by forcing the curve to intersect the origin and extrapolating the curve. Because the data are for two-way travel of the radar signal through the sand, the data were extrapolated to 50 cm to give attenuation as decibels per meter (dB/m).

2.5. Experimental results

Fig. 4 shows the decrease in backscatter with increasing sand thickness at C-band and X-band. There is an initial

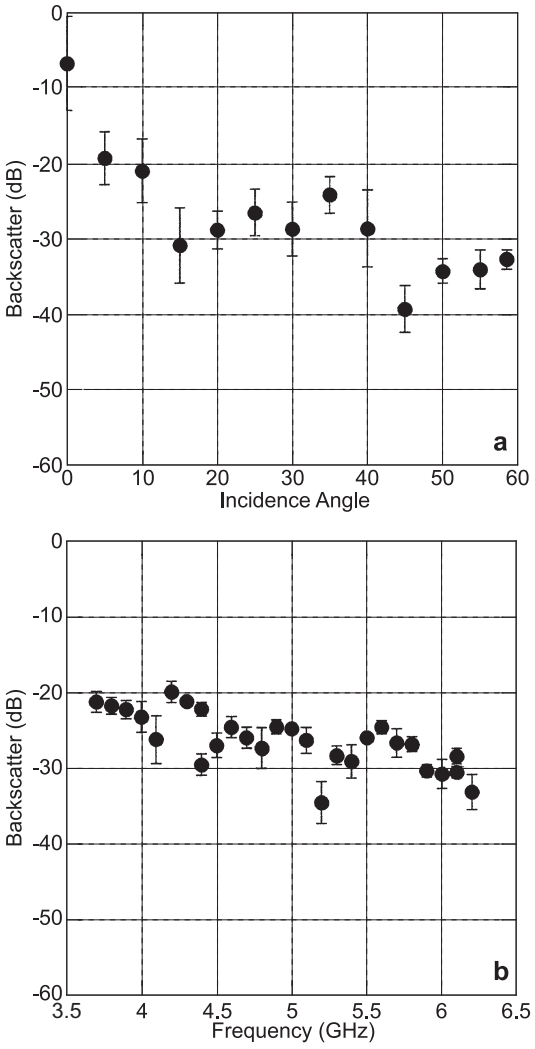

Fig. 3. (a) Example of averaged backscatter versus incidence angle for C-band (at 5.3 GHz), hh polarization, and 11.6 cm of sand. (b) Example of averaged backscatter versus frequency for C-band, hh polarization, 11.6 cm of sand, and 30° incidence angle.

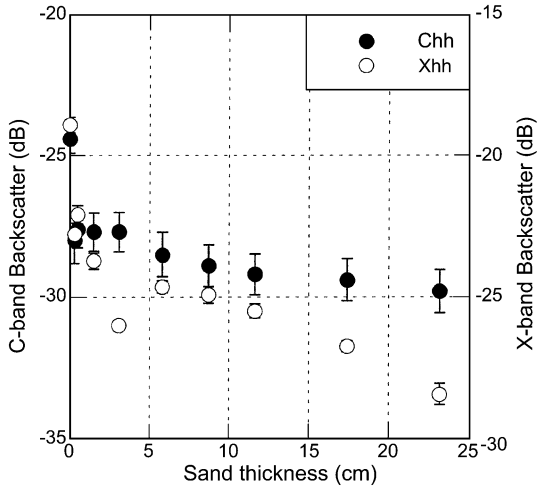

Fig. 4. Averaged backscatter versus sand thickness for C-band (5.3 GHz) and X-band (9.7 GHz), hh polarization, and 30° incidence angle. X-band data shifted by 5 dB along the *y*-axis to demonstrate greater decrease in backscatter at X-band compared to C-band.

decrease in backscatter with the first level of sand (~ 0.3 cm). This sand level fills in the roughness of the gravel, creating a smoother surface and decreasing the backscatter. The decrease is ~ 2–6 dB for like-polarized data and is slightly greater at ~ 4–8 dB for cross-polarized data. After this first drop, the backscatter continues to decrease due to increased attenuation of the signal as more sand is added. Plots of further decreasing backscatter lead to calculations of attenuation.

Table 4 gives calculated values of attenuation for the six frequency-polarization combinations in the experiment. Although measurements were made over a range of frequencies, values given in Table 4 are for center frequencies of 5.3 (C-band) and 9.7 GHz (X-band). The experimental results can be compared to theoretical attenuations by using dielectric values of the sand and following the technique of Schaber et al. (1986). Attenuation length, $1/\alpha$, is calculated by

$$1/\alpha = \lambda_0/[\pi \tan\delta(\varepsilon')^{0.5}] \quad (1)$$

where α is the attenuation coefficient, wavelength, λ_0, is in meters, and $\tan\delta = \varepsilon''/\varepsilon'$ is the loss tangent (Von Hippel, 1954). Signal attenuation is then calculated by

$$\text{attenuation} = 8.686\alpha. \quad (2)$$

Solving Eqs. (1) and (2) for C- and X-band wavelengths gives predicted attenuations of 3.4–6.8 dB/m for C-band and 6.3–12.6 dB/m for X-band. The ranges in predicted attenuations are due to the range in imaginary permittivity discussed above.

Comparison of these predicted values to the experimental results (Fig. 5) shows that the experimental results fall within the ranges of predicted attenuations. Fig. 5 also compares these results to attenuations calculated from transmission experiment measurements that used the same sand (Williams & Greeley, 2001). Attenuations calculated for C-band agree very well with the value of 4.2 dB/m calculated from transmission measurements. However, results from this backscatter experiment do not agree with the value of 5.9 dB/m for X-band calculated from transmission measurements. Because the gravel size is

Table 4
Attenuation (dB/m) as a function of frequency[a] and polarization calculated from backscatter measurements in this study

Chh	Chv	Cvv	Xhh	Xhv	Xvv
5.2 ± 1.2	4.2 ± 1.5	3.4 ± 0.5	9.9 ± 1.4	12.2 ± 1.0	10.2 ± 2.6

[a] For center frequencies of 5.3 and 9.7 GHz for C-band and X-band, respectively.

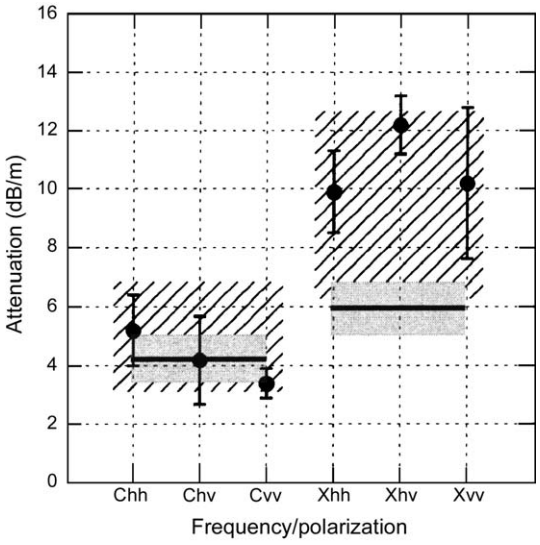

Fig. 5. Calculated attenuation values for C-band and X-band polarization combinations compared to range of predicted values (diagonal lines). The solid, horizontal lines are attenuation values calculated from transmission experiments with the gray boxes denoting error bars for those calculations.

similar to the X-band wavelength, it is likely that the surface roughness of the gravel exceeds the 'rough' criterion of Peake and Oliver (1971), creating a strong specular return. This may be affecting the change in backscatter with increasing sand thickness, leading to greater calculated attenuation than would be expected if the surface were not as rough. The cause of the difference in attenuations at X-band is not known for sure, but future experiments of this type would aid in constraining the cause of this difference. By considering different surface characteristics and radar properties, experiments such as this, conducted under controlled conditions, can be used to develop models of radar backscatter over geologic surfaces in order to understand variables due to system and target parameters.

3. Field research

3.1. Overview

While developing the laboratory measurements of backscatter, field research was also planned for comparison to the laboratory results. The Dumont Dunes, Mojave Desert, California, were selected because they are accessible and contain a variety of dune forms (MacDonald, 1970). Dumont Dunes, in the Silurian Valley 55 km north of Baker, CA, are located outside of Death Valley National Monument in a recreational area used by all-terrain vehicles. Dune forms include barchan, transverse, longitudinal, and complex star dunes, with the largest reaching heights of ~ 120 m (MacDonald, 1970) (Fig. 6). The dunes formed during the last 18,000 years as multidirectional winds accumulated sand from southern Lake Manly in present-day Death Valley and from the former Lake Dumont. Accumulation of sand continues today with sand from the Armagosa River and Salt Creek (MacDonald, 1970; Smith, 1984). Although sand accumulates from multidirectional winds, net transport of the sand is northward (Smith, 1984).

The substrate beneath the dunes is a lag deposit of lake and river sediments that were deposited in this area when Lake Dumont was present (MacDonald, 1970). Since Lake Dumont desiccated, deflation of lake sediments has occurred and continues today. During fieldwork, a hole was dug to study change in sediment with depth near the surface of the study area. An 8-cm-thick layer of desert pavement (average clast size ~ 4 cm) covers the surface and serves as the substrate immediately beneath the sand. Sand and finer

Fig. 6. Dunes (~100 m high) at Dumont Dunes, CA, the field site used for comparison with laboratory results.

grained material forms a layer ~ 10 cm thick beneath the desert pavement, and a mix of gravel and fine material is found beneath that fine-grained layer. Dumont Dunes can receive rainstorms, but it is typically very arid during the hot summer months. Yearly average rainfall is ~ 9.33 cm at nearby Silver Lake, but the combined average rainfall for May to July is only 0.06 cm. The low rainfall contributes to the paucity of vegetation.

3.2. Field measurements

Fieldwork was conducted during two flights of the NASA/JPL AIRSAR instrument in 1999 and 2000. Fieldwork consisted of sand thickness measurements and surface characterization. During the 1999 flight, a rainstorm resulted in a 3–4-cm layer of sand with 4.9% water content. In 2000, the sand was extremely dry (Table 1). These two conditions allowed comparison of radar images for two different sand moisture conditions.

The first set of field measurements bracketed the AIRSAR flights on June 2, 1999. A 100 × 100-m grid was laid out and located using a differential GPS system with horizontal accuracy of ~ 1 m. Within this grid, sand thickness was measured using a probe that was pushed through the sand until underlying desert pavement was detected by resistance when the probe hit the substrate

Fig. 7. (a) Technique for measuring sand thickness. Bare gravel surface in the foreground with 5–10-cm-thick sand being measured. (b) Corner reflector used to aid in registering radar images. The hypotenuse of each side triangle is ~1.4 m.

(Fig. 7a). This technique was tested at several locations by digging through the sand to measure the depth to desert pavement, and it was confirmed that the probe accurately measured sand thickness. The grid area contained bare desert pavement surface, thin (2–10 cm) sand, and sand up to ~1 m thick. Samples of the wet sand were later heated and dried to determine that the wet layer contained 4.9% water by volume (Table 1).

A second AIRSAR flight occurred on July 22, 2000. With the hot summer temperatures in the Mojave Desert, the dune sand was extremely dry, having measured moisture content of $0.26 \pm 0.05\%$ to a depth of at least 50 cm. This value is almost identical to the moisture level of sand used in the backscatter laboratory experiment (Table 1).

During the second AIRSAR flight, another grid was set up using the GPS unit, and sand thickness was measured. To aid in matching the GPS points to the corresponding pixels on the radar images, eight corner reflectors were emplaced prior to the flight (Fig. 7b). Although these corner reflectors were not of calibration quality, their locations showed very well in the AIRSAR images. Other features such as bushes, prominent dunes, and roads were also recorded with the GPS unit.

3.3. AIRSAR data

AIRSAR is a NASA/JPL radar imaging system that flies on a DC-8 aircraft and operates in several modes (Lou et al., 2001). For this study, polarimetric radar data (Fig. 8) were to be acquired at P-, L-, and C-bands ($\lambda = 68$, 23.5, and 5.8 cm, respectively). During the 1999 flight, P-band data were not collected because of military operations; however, data were acquired at all three bands during the 2000 flight. Slight differences in image characteristics between the two flights resulted from system configurations and from flight constraints imposed by nearby Fort Irwin, CA (Table 5).

Table 5
Radar image characteristics from AIRSAR flights over Dumont Dunes

Image ID	Date acquired	Bands	Range pixel size (m)	Along-track pixel size (m)	Angles[a] (°)
cm6088	June 2, 1999	C, L	3.32	4.58	43–57
cm6093	June 2, 1999	C, L	3.32	4.61	49–57
cm6243	July 22, 2000	C, L, P	6.64	9.22	48–59
cm6244	July 22, 2000	C, L, P	6.64	9.16	55–59

[a] Range of incidence angles that cover dune field.

3.4. Field results

Positions of corner reflectors and bushes were used to register the AIRSAR images to the map-projected GPS data. Once matched to the GPS points, backscatter values within the sand thickness measurement grids were extracted from the images and converted into decibels

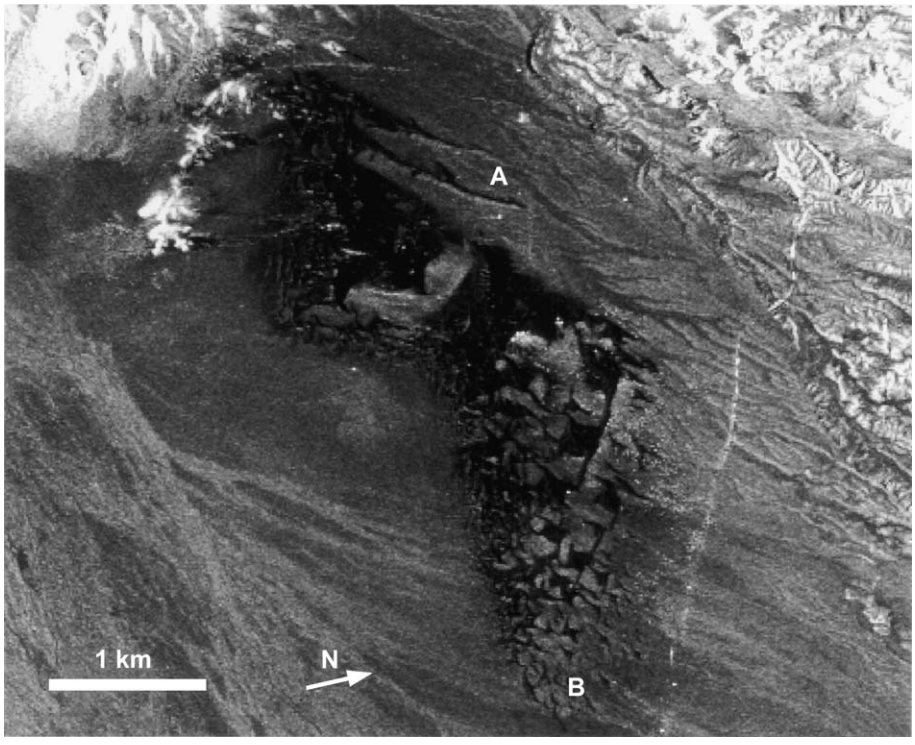

Fig. 8. Portion of L-band total power AIRSAR image. Dunes appear dark because of signal attenuation by the sand. Sand ridges shown in Fig. 11 are at A. Area of sand thickness measurements shown in Figs. 7a and 9 is at B. Illumination is from the left. Incidence angle is 55° at the left side of the dune field and 59° at the right side [AIRSAR image cm6244].

using the ENVI software package from Research Systems Inc. GPS data of other features such as dune outlines were used to verify the correct positions of the AIRSAR pixels (e.g., Fig. 9).

To search for a relationship between AIRSAR data and sand thickness, backscatter values were plotted versus sand thickness measured in the corresponding grid section. An example is shown by the open squares in Fig. 10. The scatter in the points and the large error bars are likely caused by variations in sand thickness within a grid cell or by a bush within a cell. There does not appear to be a strong relationship between backscatter and sand thickness; however, the scatter in thickness caused by irregularities may be masking a relationship.

One objective of this study was to investigate whether laboratory backscatter results can be used to predict sand thickness from backscatter image data. In order to test this, attenuation was extracted from laboratory results corresponding to the parameters for a certain image. For example, the backscatter values shown in Fig. 10 were taken from a C-band, hh polarization AIRSAR image where the incidence angle at the measurement location was 58°. The laboratory attenuation for these parameters is 6.6 dB/m. It should be noted that this value differs from that given for Chh in Table 4 because those values were corrected for signal refraction and averaged to give values that could be applied to any angle. The value of 6.6 dB/m used here was calculated from laboratory measurements at a 58° incidence angle. The attenuation is applied to the backscatter for bare ground (-19.5 dB in Fig. 10) to calculate the sand thickness at lower backscatter values. The values of predicted sand thickness are shown as a solid line in Fig. 10 where the two-way travel of the radar signal within the sand has been taken into account. The 'bare ground' in this area was composed of gravel mixed with sand, much like the

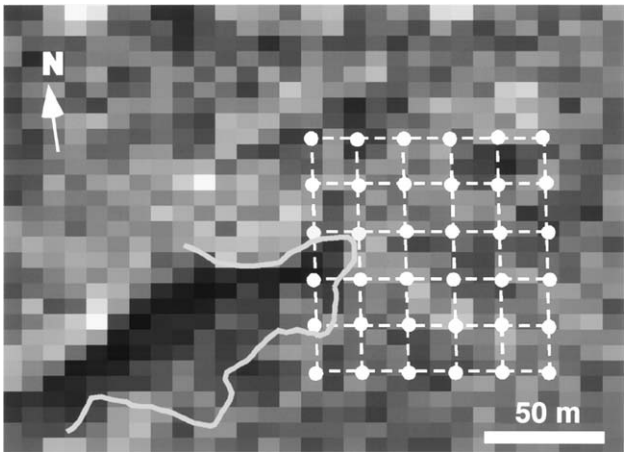

Fig. 9. Portion of an AIRSAR L-band HH backscatter image overlaid with GPS data of measurement grid and dune outline. The toe of the dune in the left part of the measurement grid is up to 1 m thick. Lower part of the grid contains bare gravel, and sand of intermediate thickness occupies other grid areas. This location is to the left of B in Fig. 8. Incidence angle is 58°, and illumination is from the bottom [AIRSAR image cm6244].

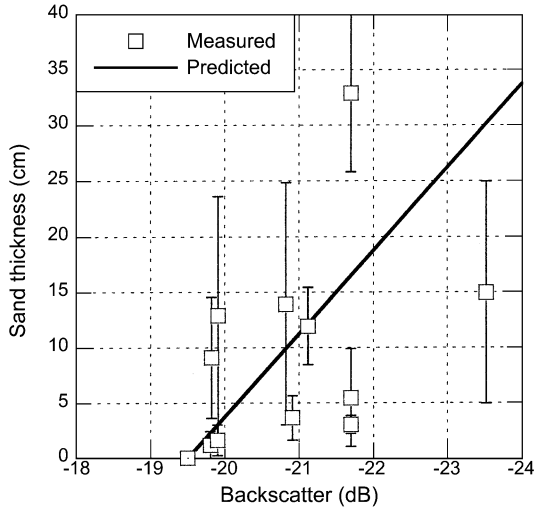

Fig. 10. Comparison of predicted and measured sand thickness shown as a function of backscatter. Open squares are sand thickness measured in the field versus backscatter values measured from an AIRSAR image. Solid line is predicted sand thickness from laboratory results using C-band radar parameters specific to this example area.

first two levels of sand in the laboratory measurements. Therefore, an initial decrease of ~ 3 dB (Fig. 4) was not applied to the predicted values in Fig. 10.

Fig. 10 shows that the measurements of sand thickness are scattered around the line of predicted thickness, but except for two outliers, most of the measured points are within 5 or 10 cm of the predicted values. This suggests that laboratory measurements of attenuation may be useful for estimating sand thickness from radar image data. However, more comparisons of predictions to field data are necessary to confirm a definite relationship.

The fieldwork also allowed ground truth for comparison of radar imagery of sand dunes under wet and dry conditions. Some areas in the 1999 images were interesting because they contain thin sand but showed as dark in some of the radar images. It was speculated that the dark radar signature was caused by increased attenuation due to wet sand and that those areas should be brighter in images acquired in 2000 when the sand was dry. Locations of these areas were noted in the 1999 AIRSAR images and were visited in 2000 to characterize the surface. It was confirmed that these areas contained ~ 1–6 cm of sand where moisture in 1999 caused greater attenuation at C-band. The moisture caused increased attenuation in both C- and L-bands, but some penetration by L-band occurred in areas of thin sand. The moisture also caused sides of some dunes to appear radar bright in L-band, likely due to small local incidence angles returning a bright signal from the sand. Many of these larger dunes appear radar dark in the 2000 images because the signal passed into the dry sand and was attenuated. In the 2000 images, extent of dry sand is shown better in C-band because sand of intermediate thickness (few tens of centimeters) attenuated the signal. The L- and P-band

signals penetrated this sand and give a brighter return, but thicker sand still attenuates the radar signals and shows as radar dark (Fig. 11). In the 1999 images, sand attenuated the C-band signal, but L-band was able to penetrate the moist sand where it was up to a few tens of centimeters thick (Fig. 11).

Overall, C-band images are useful for determining the extent of sand in an area, and L-band images can be used to discern the dune morphologies. P-band signals (and perhaps some L-band signals) likely penetrated the desert pavement into the subsurface gravel of the lake deposits. The penetration into the subsurface in this very dry area by P-band signals cannot be quantified because required field measurements were not made. Although Dumont Dunes offers an accessible area with interesting dune morphologies, the subsurface is largely unconsolidated, promoting penetration by lower frequency radars. Future field measurements coordinated with radar image acquisition should be conducted in areas where the substrate is bedrock.

4. Conclusions

Laboratory measurements of radar backscatter were made over a surface of gravel in order to measure the change in backscatter with increasing thickness of a sand cover. These measurements were made at various polarizations and incidence angles for C-band and X-band, and the change in backscatter was used to calculate attenuation caused by sand (Table 4). The attenuation values calculated here agree well with values measured in microwave trans-

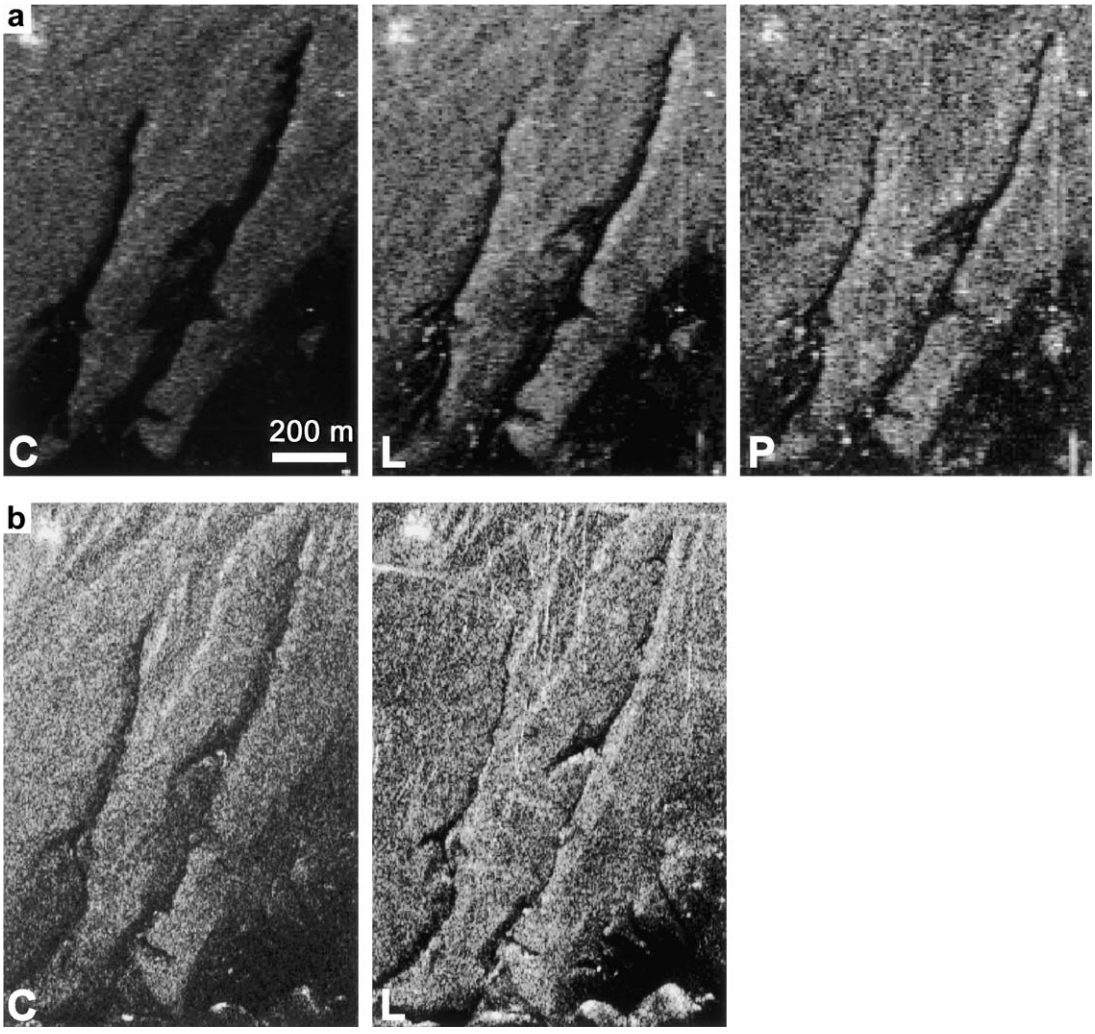

Fig. 11. (a) Portion of AIRSAR image cm6244 from 2000 at C-, L-, and P-bands, total power. These dry sand ridges are shown at A in Fig. 8 and are 2–4 m high. Note that the ridges appear wider in C-band because there is more attenuation of the signal. The ridges are narrowest in P-band because of greater signal penetration. Incidence angle is 56°, and illumination is from the bottom. (b) Portion of AIRSAR image cm6093 from 1999 showing sand ridges in C- and L-bands (total power) when sand was moist (4.9% H_2O). Note that C-band again attenuates more signal, but L-band appears to have still penetrated thin areas of the wet sand. Incidence angle is 53°, and illumination is from the bottom.

mission experiments at C-band but are almost twice the attenuation at X-band measured by transmission. This disagreement at X-band may be due to Rayleigh scattering effects of the gravel, but it would be worthwhile to test this in future experiments.

The laboratory measurements also showed an initial decrease in backscatter of 2–8 dB when a thin layer of sand filled spaces within the gravel. This steep drop in backscatter was caused by smoothing of initial surface roughness by sand. As sand was added to greater thickness, the backscatter continued to decrease due to increased attenuation.

Field measurements of sand thickness were compared to thickness estimates based on AIRSAR backscatter and laboratory results. Although there is general agreement between predicted and measured sand thickness values, scatter in measured sand thickness caused by nonuniform sand and sparse vegetation makes it difficult to determine definitely whether there is a relationship. However, future additional comparisons of laboratory results to field measurements may answer this question.

Fieldwork was also used to ground truth causes of differences between AIRSAR images of dry and wet sand. Fig. 11 shows dependence of thin sand backscatter on wavelength for dry and wet sand. The extent of the dry sand coverage is shown well in the C-band images, but L- and P-bands penetrate thin sand. L-band is better for determining dune morphologies. P-band shows the locations of thicker sand when compared with L-band and may have penetrated into the subsurface. When the sand was wet, the C-band signal was attenuated, but L-band appears to have penetrated thin sand even though it was wet. The ability of L-band (and presumably P-band if it were available) to penetrate thin wet sand without great attenuation agrees with microwave transmission experiments (Williams, 2002; Williams & Greeley, 2001). Although penetration would be greater in dry sand, these results challenge previous allegations that sand must be extremely dry for radar penetration to occur.

As future imaging radar missions are developed, it is important to consider results of studies such as this that combine field measurements and laboratory data to construct a better understanding of the ability of radar to penetrate sand at various radar parameters and under different surface conditions.

Acknowledgements

The authors wish to acknowledge C. Birtcher and G. Beardmore for their assistance with the experiment and R. Davis, M. Kraft, and J. Moreau for help in the field. We thank E. O'Leary and the AIRSAR team for acquiring the radar images of the field site. We also thank J. van Zyl and T. Farr for helpful discussions, D. Ball for photographic support, and C. Santamarina for conducting the dielectric measurements. We are grateful for reviews by T. Farr and an anonymous reviewer that improved this manuscript. This work was supported by a NASA GSRP fellowship through JPL, a NASA/ASU Space Grant fellowship, and the Dr. Robert H. Goddard Scholarship from the National Space Club.

References

Berlin, G. L., Tarabzouni, M. A., Al-Naser, A. H., Sheikho, K. M., & Larson, R. W. (1986). SIR-B subsurface imaging of a sand-buried landscape: Al Labbah Plateau, Saudi Arabia. *IEEE Transactions on Geoscience and Remote Sensing*, *GE-24*, 595–602.

Birtcher, C. R., 1992. *The electromagnetic anechoic chamber at Arizona State University: Characterization and measurements*. *M.S. thesis*. Tempe: Arizona State University, 120 pp.

Blom, R. G., Crippen, R. E., & Elachi, C. (1984). Detection of subsurface features in SEASAT radar images of Means Valley, Mojave Desert, California. *Geology*, *12*, 346–349.

Breed, C. S., Schaber, G. G., McCauley, J. F., Grolier, M. J., Haynes, C. V., Elachi, C., Blom, R., Issawi, B., & McHugh, W. P. (1983). Subsurface geology of the Western Desert in Egypt and Sudan revealed by Shuttle Imaging Radar (SIR-A). *First Spaceborne Imaging Radar Symposium, JPL Pub. 83-11* (pp. 10–12). Pasadena, CA: Jet Propulsion Laboratory.

Campbell, B. A., Campbell, D. B., Grant, J. A., Hensley, S., Maxwell, T. A., Plaut, J. J., Rosen, P., Shepard, M. K., & Simpson, R. (2001). Orbital imaging radar and the search for water on Mars. *Conference on Geophysical Detection of Subsurface Water on Mars, Abstract #7040*. Houston: Lunar and Planetary Institute.

Dabbagh, A. E., Al-Hinai, K. G., & Khan, M. A. (1997). Detection of sand-covered geologic features using SIR-C/X-SAR data. *Remote Sensing of Environment*, *59*, 375–382.

Davis, P. A., Breed, C. S., McCauley, J. F., & Schaber, G. G. (1993). Surficial geology of the Safsaf region, south-central Egypt, derived from remote sensing and field data. *Remote Sensing of Environment*, *46*, 183–203.

Dellwig, L. F. (1969). An evaluation of mutifrequency radar imagery of the Pisgah Crater area, California. *Modern Geology*, *1*, 65–73.

Elachi, C., Roth, L. E., & Schaber, G. (1984). Spaceborne radar subsurface imaging in hyperarid regions. *IEEE Transactions on Geoscience and Remote Sensing*, *GE-22*, 383–387.

Farr, T. G., Elachi, C., Hartl, P., & Chowdhury, K. (1986). Microwave penetration and attenuation in desert soil: A field experiment with the Shuttle Imaging Radar. *IEEE Transactions on Geoscience and Remote Sensing*, *GE-24*, 590–594.

Jordan, R. L., Huneycutt, B. L., & Werner, M. (1995). The SIR C/X SAR synthetic aperture radar system. *IEEE Transactions on Geoscience and Remote Sensing*, *33*, 829–839.

Lou, Y., Imel, D. A., Chu, D., Miller, T. W., Moller, D., & Skotnicki, W. (2001). Progress report on the NASA/JPL Airborne Synthetic Aperture Radar system. *IEEE IGARSS '01* (pp. 2046–2048). Piscataway, NJ: IEEE.

MacDonald, A. A. (1970). The northern Mojave Desert's Little Sahara. *Mineral Information Service, vol. 23* (pp. 3–6). Sacramento: CA Division of Mines and Geology.

McCauley, J. F., Breed, C. S., Schaber, G. G., McHugh, W. P., Issawi, B., Haynes, C. V., Grolier, M. J., & Kilani, A. E. (1986). Paleodrainages of the Eastern Sahara—The radar rivers revisited (SIR-A/B implications for a mid-Tertiary trans-African drainage system). *IEEE Transactions on Geoscience and Remote Sensing*, *GE-24*, 624–648.

McCauley, J. F., Schaber, G. G., Breed, C. S., Grolier, M. J., Haynes, C. V., Issawi, B., Elachi, C., & Blom, R. (1982). Subsurface valleys and geo-

archaeology of the eastern Sahara revealed by shuttle radar. *Science*, *218*, 1004–1020.

Nesti, G., Fortuny, J., & Lopez-Sanchez, J. M. (2000). Polarimetric microwave remote sensing experiments at the EMSL. *IEEE Geoscience and Remote Sensing Society Newsletter*, *113*, 6–11.

Peake, W. H., & Oliver, T. L. (1971). *The response of terrestrial surfaces at microwave frequencies*. Ohio State University Technical Report 2440-7, Columbus, OH.

Saunders, R. S., et al. (1992). Magellan mission summary. *Journal of Geophysical Research*, *97*, 13067–13090.

Schaber, G. G., & Breed, C. S. (1999). The importance of SAR wavelength in penetrating blow sand in northern Arizona. *Remote Sensing of Environment*, *69*, 87–104.

Schaber, G. G., McCauley, J. F., Breed, C. S., & Olhoeft, G. R. (1986). Shuttle imaging radar: Physical controls on signal penetration and scattering in the eastern Sahara. *IEEE Transactions on Geoscience and Remote Sensing*, *GE-24*, 603–623.

Smith, R. S. U. (1984). Eolian geomorphology of the Devil's Playground, Kelso Dunes, and Silurian Valley, California. *Geological Society of America, 97th, Field Trip 14* (pp. 162–174). Boulder, CO.

Von Hippel, A. R. (1954). *Dielectrics and waves* (pp. 26–37). New York: Wiley.

Williams, K. K. (2002). *Radar penetration of sand and dust as determined by laboratory and field measurements*. *Ph.D. Thesis*. Tempe, AZ: Arizona State University.

Williams, K. K., & Greeley, R. (2001). Radar attenuation by sand: Laboratory measurements of radar transmission. *IEEE Transactions on Geoscience and Remote Sensing*, *39*, 2521–2526.